

# A strong lateral shear velocity gradient and anisotropy heterogeneity in the lowermost mantle beneath the southern Pacific

Sean R. Ford,<sup>1,2</sup> Edward J. Garnero,<sup>1</sup> and Allen K. McNamara<sup>1</sup>

Received 10 December 2004; revised 27 July 2005; accepted 5 October 2005; published 9 March 2006.

[1] Velocity heterogeneity and seismic anisotropy in the D'' region beneath the southern Pacific Ocean is investigated using broadband shear waves from southwest Pacific and South American earthquakes recorded by permanent and temporary stations in Antarctica, Australia, South America, and on islands in the South Pacific. Shear velocity perturbations ( $\delta V_S$ ) are inferred from the differential travel times between hand-picked horizontally polarized (SH) direct or diffracted S arrivals and vertically polarized (SV) SKS arrivals. Derived patterns in  $\delta V_S$  roughly agree with global shear velocity models but reveal a stronger shear velocity lateral gradient north of approximately 52°S where  $\delta V_S$  transitions from approximately +0.5 to -1.0% (relative to radially averaged reference models) over less than 600 km along the base of D''. Waveform analyses provide an even stronger constraint on the transitional region, where there is a change in waveform behavior occurring over length scales less than 300 km. Differential travel times between SKKS and SKS, calculated by cross-correlating SKS with Hilbert transformed SKKS, support large  $\delta V_S$  amplitudes and help to constrain the location of the transitional region. Anisotropy in D'' ( $k_S$ ) is inferred from handpicked differential travel times between the SV and SH components of direct or diffracted S and display a slight spatial trend where the SH component precedes the SV in the north and east of the study area but arrives after SV in the center and southwest of it. However, there is high  $k_S$  variability in the center of the study region. There is no apparent correlation between  $\delta V_S$  and  $k_S$ . Abrupt changes in the character of velocity and anisotropy in this region of D'' may be related to chemical heterogeneity at the boundary of the Pacific Superswell, as well as small-scale convection in the deep mantle.

**Citation:** Ford, S. R., E. J. Garnero, and A. K. McNamara (2006), A strong lateral shear velocity gradient and anisotropy heterogeneity in the lowermost mantle beneath the southern Pacific, *J. Geophys. Res.*, 111, B03306, doi:10.1029/2004JB003574.

## 1. Introduction

[2] The deep mantle region directly above the core-mantle boundary (CMB) is known as D'' [Bullen, 1949] and plays a major role in the dynamics of Earth's mantle [e.g., Lay et al., 1998b; Tackley, 2000] and core [e.g., Christensen and Olson, 2003; Glatzmaier, 2002]. It is the lower boundary layer in the convecting mantle and blankets the liquid iron core. Thus D'' rests above the greatest absolute density change in Earth and continues to attract great interest in the Earth and planetary interior research community.

[3] The best means of directly investigating D'' is with seismic methods, and recent studies find lateral velocity heterogeneity in D'' on a variety of scales (e.g., see review

by Garnero [2000]). Relatively large scale (500–3000 km) three-dimensional (3-D) heterogeneity is elucidated by global seismic tomography [e.g., Antolik et al., 2003; Grand, 2002; Masters et al., 2000; Mégnin and Romanowicz, 2000; Ritsema and van Heijst, 2000]. Regional studies of differential travel times are often employed to illuminate strong heterogeneity at small scales (10–1000 km) [e.g., Fisher et al., 2003; Garnero et al., 1993; Ritsema et al., 1997; Russell et al., 1999; Vidale and Hedlin, 1998; Wysession et al., 2001]. A similar situation exists for investigations of D'' anisotropy. Regional studies highlight small-scale variations (e.g., see reviews by Kendall [2000] and Lay et al. [1998a]), while efforts to characterize global D'' anisotropy are restricted to much larger scales (>2000 km) (M. P. Panning and B. A. Romanowicz, A three-dimensional radially anisotropic model of shear velocity in the mantle, submitted to *Geophysical Journal International*, 2005, hereinafter referred to as Panning and Romanowicz, submitted manuscript, 2005).

[4] The locations of regional studies of seismic anisotropy and velocity heterogeneity are restricted by earthquake and seismic station distribution, and several dynamically

<sup>1</sup>Department of Geological Sciences, Arizona State University, Tempe, Arizona, USA.

<sup>2</sup>Now at Department of Earth and Planetary Science, University of California, Berkeley, California, USA.

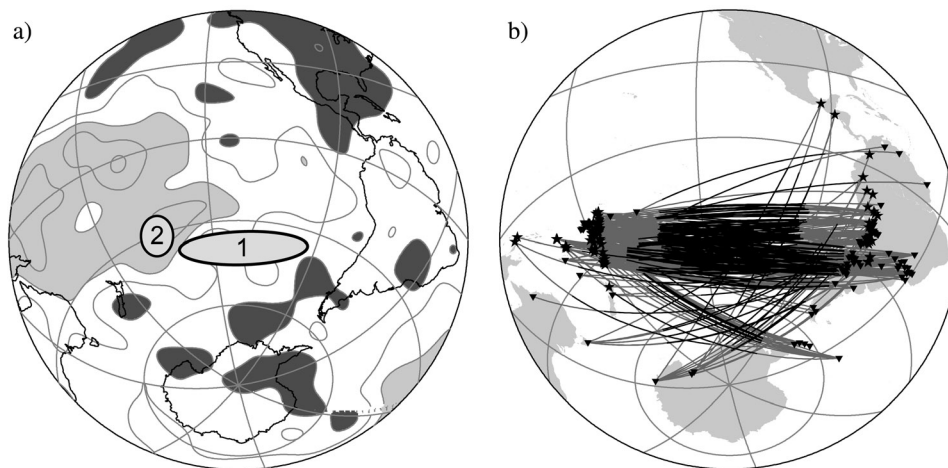


**Figure 1.** (a) Shear velocity perturbations relative to PREM, from the tomographic model SAW24B16 [Méglin and Romanowicz, 2000]. Areas with  $\delta V_S > 1\%$  have darker shading, and  $\delta V_S < -1\%$  are lightly shaded; 1% contour intervals (grey lines) are shown, and the map is a Lambert azimuthal equal-area hemisphere projection. Region 1 is the narrow corridor studied by Kendall and Silver [1996a], and region 2 is the low-velocity anomaly inferred by Tanaka [2002]. (b) Stations (triangles), events (stars), great circle projections of ray paths (grey lines), and great circle projections of the PREM-calculated ray paths in a 300 km thick D'' (thick black lines) used in this study are shown on the same projection as Figure 1a.

interesting areas of the lowermost mantle have yet to be probed due to this limitation. One such area of relatively poor coverage is the southern Pacific. Tomographic inversions characterize the long-wavelength signature of the southern Pacific as a region in transition from low shear velocities in the north/northwest through average velocities in the center to high velocities in the south/southwest (e.g., Figure 1a). However, because of the paucity of data, the southern hemisphere is resolved with less confidence than the northern hemisphere [Vasco *et al.*, 2003]. While past studies have highlighted structure in neighboring regions, the lower mantle beneath the southern Pacific has not been explored in great detail. Notable exceptions are the detection of anisotropy in a narrow east-west strip along the middle of our extended study region by Kendall and Silver [1996a] (Figure 1a, region 1), and a study of *S-SKS* and *SKKS-SKS* differential travel times by Tanaka [2002] that proposed the presence of a very low shear velocity region in the northwest of our study area (Figure 1a, region 2). Both studies utilized relatively small data sets. The recent proliferation of portable seismic station deployments in South America and the southwest Pacific, however, has greatly improved coverage in the southern Pacific (Figure 1b), and a thorough study of D'' using direct and diffracted *S* waves (hereinafter referred to jointly as *S*) is now possible.

[5] In this paper we focus on characterizing intermediate to small-scale (100–500 km) velocity and anisotropy heterogeneity in the southern Pacific. We investigate whether the low-velocity anomalies in our study region are similar to those in the southern Atlantic and Africa, which have been shown to possess travel time anomalies characteristic of low-velocity material with sharp edges [Ni *et al.*, 2002; Wen, 2001]. Such a similarity would suggest a thermochemical origin of wave speed depressions in our study region. We present both travel time and waveform analyses in an

effort to better understand the chemical, rheological, and dynamical nature of the southern Pacific.

## 2. Data Set

[6] We gathered broadband digital seismic data of earthquakes with source depths greater than 100 km, event magnitudes greater than 5.6, and epicentral distances between  $85^\circ$  and  $125^\circ$ . Instrument responses were deconvolved from the data to obtain displacement seismograms, then band-pass filtered between 1 and 100 s with a second-order Butterworth filter. The traces were rotated to the great circle reference frame to obtain radial and transverse components of motion; and the resultant radial and vertical components were then rotated to the reference frame of incident *S* ray paths using the one-dimensional (1-D) PREM 1 Hz reference velocity model [Dziewonski and Anderson, 1981]. This second rotation helps to minimize any possible *SV*-to-*P* energy conversion generated from the Moho (or other discontinuities) that may contribute to either precursors or distortions of the *SV* component of *S* ( $S_{SV}$ ). We selected data with high signal-to-noise ratios and simple source time functions as evidenced by impulsive *SKS* signals. Our criteria were met by 276 records in the seismic velocity analysis and 170 records in the seismic anisotropy analysis (Figure 1b). The records were of 83 events (Table 1) recorded at 87 permanent and temporary stations (Table 2). Nearly half of our recordings came from temporary arrays, which made it possible to examine this study region more completely than permanent networks alone would permit. Additionally, temporary seismometer deployments are often geographically concentrated, resulting in dense, subregional sampling of D'' structure (Figure 2).

[7] Though the ray paths of our data are predominately along an east-west striking azimuth (Figure 1b), we are fortunate to have events and stations on both sides of the

**Table 1.** Event Information From USGS Catalogue for Data Used in This Study

Event	Date, yyyymmdd	Latitude, deg	Longitude, deg	Z, km	$m_b$	$\delta V_s^a$ %	$ks^b$ %
1	19910623	-26.80	-63.35	558	6.4	1	1
2	19910706	-13.11	-72.19	104	6.5	1	0
3	19921112	-22.40	-178.10	359	5.9	3	3
4	19930416	-17.78	-178.86	565	6.9	4	4
5	19930424	-17.87	179.85	599	6.3	0	1
6	19930524	-22.67	-66.54	221	7.0	1	0
7	19930807	-23.87	179.85	523	6.7	6	4
8	19940110	-13.34	-69.45	596	6.9	7	6
9	19940211	-18.77	169.17	205	6.9	2	1
10	19940309	-18.04	-178.41	562	7.6	16	12
11	19940331	-22.06	-179.53	579	6.5	9	6
12	19940429	-28.30	-63.25	561	6.9	5	3
13	19940510	-28.50	-63.10	600	6.9	4	4
14	19940609	-13.84	-67.55	631	8.2	8	3
15	19940811	-21.84	-176.71	179	5.9	1	1
16	19940819	-26.64	-63.42	563	6.5	1	0
17	19941027	-25.78	179.34	518	6.7	15	6
18	19941212	-17.48	-69.60	148	6.3	1	1
19	19941227	-31.97	179.86	212	6.4	2	0
20	19950117	-20.83	-179.24	633	6.3	4	0
21	19950623	-24.56	-177.26	108	5.8	1	0
22	19950629	-19.54	169.29	139	6.9	6	7
23	19950814	-4.84	151.51	127	6.7	2	0
24	19950825	-18.69	-175.41	224	6.0	1	1
25	19951006	-20.00	-175.92	197	6.4	2	1
26	19951014	-25.76	-177.52	147	6.2	2	2
27	19951021	16.84	-93.47	159	7.2	2	0
28	19960416	-24.06	-177.04	110	7.2	5	1
29	19960805	-20.69	-178.31	550	7.4	2	2
30	19961019	-20.41	-178.51	590	6.9	1	1
31	19961105	-31.16	180.00	369	6.8	4	2
32	19961114	-21.24	-176.62	191	6.2	1	1
33	19961201	-30.52	-179.68	355	6.2	1	0
34	19970103	-19.22	-174.84	140	6.0	1	0
35	19970123	-22.00	-65.72	276	7.1	3	1
36	19970321	-31.16	179.62	448	6.3	4	2
37	19970412	-28.17	-178.37	183	6.0	3	2
38	19970525	-32.12	179.79	332	7.2	8	5
39	19970904	-26.57	178.34	624	6.8	3	1
40	19971014	-22.10	-176.77	167	7.8	5	0
41	19971017	-20.89	-178.84	578	6.0	2	1
42	19971028	-4.37	-76.68	112	7.2	2	0
43	19971103	-19.96	-175.36	151	5.9	2	1
44	19971109	13.85	-88.81	176	6.5	1	0
45	19971115	-15.15	167.38	123	7.0	2	0
46	19971128	-13.74	-68.79	586	6.7	3	1
47	19971211	3.93	-75.79	177	6.4	1	1
48	19971218	13.84	-88.74	182	6.1	1	0
49	19980126	-22.04	-176.84	159	5.7	1	1
50	19980127	-22.54	179.05	611	6.3	2	2
51	19980329	-17.55	-179.09	537	7.2	4	3
52	19980403	-8.15	-74.24	164	6.6	2	1
53	19980414	-23.82	-179.87	498	6.1	4	3
54	19980516	-22.23	-179.52	586	6.9	5	5
55	19980709	-30.49	-178.99	129	6.9	3	2
56	19981227	-21.63	-176.38	144	6.8	1	1
57	19990119	-4.60	153.24	114	7.0	1	0
58	19990413	-21.42	-176.46	164	6.8	2	1
59	19990915	-20.93	-67.28	218	6.4	1	0
60	19991025	-38.70	175.80	158	6.2	0	2
61	19991130	-18.90	-69.17	128	6.6	2	2
62	19991207	-15.91	-173.98	137	6.4	1	2
63	20000108	-16.92	-174.25	183	7.2	4	3
64	20000113	-17.61	-178.74	535	6.2	2	2
65	20000212	-15.89	-174.80	226	5.9	1	1
66	20000423	-28.31	-62.99	608	7.0	7	4
67	20000504	-17.91	-178.52	515	6.5	1	0
68	20000512	-23.55	-66.45	225	7.2	5	2
69	20000614	-25.52	178.05	604	6.4	1	1
70	20000616	-33.88	-70.09	120	6.4	1	1
71	20000815	-31.51	179.73	357	6.6	2	1

**Table 1.** (continued)

Event	Date, yyyymmdd	Latitude, deg	Longitude, deg	Z, km	$m_b$	$\delta V_s^a$ %	$ks^b$ %
72	20000911	-15.88	-173.69	115	6.3	1	1
73	20001218	-21.18	-179.12	628	6.7	1	1
74	20010109	-14.93	167.17	103	7.1	11	6
75	20010428	-18.06	-176.94	351	6.9	3	3
76	20010603	-29.67	-178.63	178	7.2	17	8
77	20010704	-21.73	-176.71	184	6.5	3	2
78	20020508	-17.95	-174.57	130	6.2	10	10
79	20021004	-20.99	-179.02	621	6.3	1	2
80	20021012	-8.30	-71.74	534	6.9	2	2
81	20021022	-20.63	-178.39	549	6.2	2	2
82	20030104	-20.57	-177.66	378	6.5	2	2
83	20031106	-19.26	168.89	113	6.6	1	1

<sup>a</sup>Number of observations in velocity heterogeneity analysis.<sup>b</sup>Number of observations in anisotropy heterogeneity analysis.

southern Pacific to produce reciprocal ray paths. However, similar to other D'' velocity and anisotropy heterogeneity studies, we suffer from limited azimuthal sampling. Nonetheless, in the following sections, we demonstrate that details in the travel time and waveform analyses permit characterization of structure at relatively short scales in the center of our study region, particularly in the north-to-south direction.

### 3. Shear Wave Velocity Heterogeneity

#### 3.1. S-SKS Differential Travel Time Residuals

[8] The arrival times of *SKS* and the *SH* component of *S* ( $S_{SH}$ ) were measured by hand-picking the phase onset on the radial and transverse component, respectively (Figure 3a). We retained measurements for which the individual *SKS* and  $S_{SH}$  arrival times could be picked within  $\pm 0.5$  s accuracy. Depth phases can interfere with *S*, greatly degrading timing accuracy and phase identification confidence (see auxiliary material<sup>1</sup>). To prevent this, we identified (when present) *sSKS*, *sSKKS*, *pSKS*, and *pSKKS* arrivals in distance profiles, and discarded any records where these depth phases interfere with *S* (or  $S_{diff}$ ). We subtracted isotropic PREM-predicted *S-SKS* differential travel times from the observed  $S_{SH-SKS}$  differential travel times to obtain *S-SKS* differential travel time residuals ( $\delta T_{S-SKS}$ ). Measurement of the peak-to-peak times of *SKS* and  $S_{SH}$  by hand picking or cross correlation was not used to obtain differential travel times due to the difference in frequency content between the two phases, as well as waveform variability of the diffracted *S* wave. We did not pursue the measurement of  $S_{SH-SKS}$  differential travel times via cross correlation with synthetic seismograms because our data contained so many different source time functions and instrument responses, which made the task of creating appropriate synthetics impractical.

[9] The  $\delta T_{S-SKS}$  were also corrected for the aspherical Earth structure predicted from the shear wave tomography models, SAW24B16 [Méglin and Romanowicz, 2000], TXBW [Grand, 2002], and S20RTS [Ritsema and van Heijst, 2000]. *S* was corrected throughout the mantle down to a depth of 2591 km (300 km thick D''), and *SKS* from the surface to the CMB. These corrections are intended to minimize the possible effect of mapping heterogeneity elsewhere in the mantle into D'' structure. Here we do not

<sup>1</sup>Auxiliary material is available at <ftp://ftp.agu.org/apend/jb/2004JB003574>.

**Table 2.** Information on Seismic Networks and Arrays for Data Used in This Study

Data Source <sup>a</sup>	Array	Stations	Records	Upper Mantle Anisotropy Correction Reference
IRIS	GEOSCOPE	5	42	<i>Barruol and Hoffmann</i> [1999]
IRIS	GeoForschungsNetz (GEOFON)	1	1	<i>Bock et al.</i> [1998]
IRIS	Global Telemetered Southern Hemisphere Network (GTSN)	6	59	<i>Russo and Silver</i> [1994] and <i>Helffrich et al.</i> [2002]
IRIS	International Deployment of Accelerometers (IDA)	3	22	<i>Helffrich et al.</i> [2002], <i>Fischer and Wiens</i> [1996], and <i>Vinnik et al.</i> [1992]
IRIS	U.S. Geological Survey (USGS)	9	28	<i>Audoine et al.</i> [2000] and <i>Helffrich et al.</i> [2002]
PASSCAL	Southwest Pacific Seismic Experiment (SPaSE)	8	15	<i>Fischer and Wiens</i> [1996]
PASSCAL	Seismic Experiment in Patagonia and Antarctica (SEPA)	4	8	<i>Helffrich</i> [2002]
PASSCAL	Broadband Andean Joint Experiment/ Seismic Exploration of the Deep Altiplano (BANJO/SEDA)	9	14	<i>Polet et al.</i> [2000]
PASSCAL	Andean Altiplano Volcanic Complex Experiment (APVC)	3	6	<i>Leidig and Zandt</i> [2003]
PASSCAL	Chile Argentina Geophysical Experiment (CHARGE)	16	33	<i>Anderson et al.</i> [2004]
CIW	Bolivian Lithosphere Seismic Project (BLSP)	13	34	<i>James and Assumpcao</i> [1996]
CIW	Southeast Caribbean/South America Project (SECaSA)	1	1	<i>Russo and Silver</i> [1994]
GFZ	Proyecto de Investigacion Sismologica de la Cordillera Occidental (PISCO)	6	7	<i>Polet et al.</i> [2000]
NIED	South Pacific Broadband Seismic Network (SPANET)	3	7	<i>Fischer and Wiens</i> [1996]

<sup>a</sup>IRIS, Incorporated Research Institutions for Seismology; PASSCAL, Program for the Array Seismic Studies of the Continental Lithosphere; CIW, Carnegie Institution of Washington; GFZ, GeoForschungsZentrum–Potsdam; NIED, National Research Institute for Earth Science and Disaster Prevention.

attempt to correct the D'' portion of  $S$  paths (using the tomographic models) as we seek to understand heterogeneity in the D'' layer relative to a 1-D reference structure (i.e., PREM) rather than any particular 3-D model. Our choice of a 300 km thickness of the D'' layer is arbitrary, and may bias the strength of estimated heterogeneity and anisotropy. However, this bias is presumably a minor effect, as D'' path lengths are typically long for our data and are thus only slightly perturbed by a different layer thickness. The  $\delta T_{S-SKS}$  range from  $-5.6$  to  $15.6$  s (Figure 4a), and, when averaged in epicentral distance bins, show a slight increase with distance. However, travel times are significantly scattered around these averages, suggesting the presence of lateral variations in the shear velocity structure. The range of  $\delta T_{S-SKS}$  found in this study is consistent with the global data set of *Kuo et al.* [2000].

### 3.2. SKKS-SKS Differential Travel Time Residuals

[10] The  $\delta T_{S-SKS}$  were supplemented with SKKS-SKS differential travel time residuals ( $\delta T_{SKKS-SKS}$ ). SKKS is an SKS wave with an additional bounce on the underside of the CMB, and as a minimax travel time path, has a  $\pi/2$  phase shift relative to SKS [*Choy and Richards*, 1975]. Hand-picking the SKKS onset is not reliable, since its waveshape initiates with a small initial pulse that is often obscured in the noise, so the differential travel times were measured with a cross-correlation technique on a subset of our data with clear SKS and SKKS arrivals and epicentral distances greater than  $100^\circ$ . We took the Hilbert transform of the polarity-reversed, hand-windowed SKKS phase ( $-\mathcal{H}(SKKS)$ ), and cross-correlated it with the hand-windowed SKS phase. A similar technique was employed by *Tanaka* [2002].

[11] When cross-correlating SKKS and SKS one must be sensitive to neighboring arrivals in time that can contaminate or skew the measurement. SKS at around  $110^\circ$  undergoes the birth of  $SPdKS$  emerging from its shoulder, which in some cases can completely distort the SKS pulse shape [e.g., *Thorne and Garnero*, 2004]. Furthermore, SKKS has higher-order CMB underside reflections closely trailing in time, most notably SKKKS at greater distances. To address these challenges we visually inspect the radial component SKS and  $-\mathcal{H}(SKKS)$  to first assess waveform similarity. If there are interfering phases, then the window is chosen to exclude waveform distortions while maintaining a realistic SKS and  $-\mathcal{H}(SKKS)$  waveform. If this is not possible, the data are discarded.

[12] Data with an SKKS-SKS cross-correlation coefficient greater than 0.7 were kept for analysis, which resulted in 73 differential travel time measurements. The differential travel times were then referenced to PREM, as in the  $S$ -SKS analysis, to obtain  $\delta T_{SKKS-SKS}$  ranging from  $-3$  to  $5$  s (Figure 4b). The  $\delta T_{SKKS-SKS}$  are large at small epicentral distances and maintain their amplitude even after correction for 3-D mantle structure. A bias of approximately 1 s in  $\delta T_{SKKS-SKS}$  has been noted in previous work [*Liu and Dziewonski*, 1998; *Sylvander and Souriau*, 1996]. It is difficult to properly identify the source of such a bias, since it may be attributed to sources such as (1) SKKS-SKS path coverage biased in low-velocity regions, primarily the extremely well sampled Fiji-Tonga to N. America corridor; (2) unaccounted for effects from the 3-D nature of the heterogeneity, which can further increase the SKKS-SKS differential travel times [e.g., *Garnero and Helmberger*, 1995]; and (3) a bias in the outermost core structure of the reference model, which is difficult to assess at present since

*SmKS* energy used to study such structure is strongly contaminated by the often unknown D'' structure [e.g., *Sylvander and Souriau*, 1996]. Thus we make no attempt to correct for any such bias, since it is likely due to structure we wish to pursue. There is agreement in  $\delta T_{SKS-SKS}$  with the southern Pacific lower mantle shear velocity study of *Tanaka* [2002].

### 3.3. Inferred D'' Velocity Heterogeneity

[13] Velocity perturbations relative to the PREM model ( $\delta V_S$ ) were estimated by uniformly distributing tomograph-

ically corrected  $\delta T_{S-SKS}$  along their PREM-predicted ray paths in a 300 km thick D'' layer. The  $\delta V_S$  estimates allow direct comparison to other velocity models, and essentially correct the differential travel time residuals for D'' path length. This allows more confident comparison of measurements within the data set. The  $\delta V_S$  estimates range from  $-1.8\%$  to  $1.1\%$ , and are plotted at ray path midpoints in Figures 5b–5d (where the background of the plot is the velocity model used to correct  $\delta T_{S-SKS}$ ). Our  $\delta V_S$  estimates generally agree in magnitude with the shear wave velocity models, TXBW (Figure 5b), S20RTS (Figure 5c), and SAW24B16 (Figure 5d). There is an overall spatial trend of negative  $\delta V_S$  (positive  $\delta T_{S-SKS}$ ) in the northwest and positive  $\delta V_S$  (negative  $\delta T_{S-SKS}$ ) in the southeast. In the center of our study region, the location of some of the largest lateral velocity gradients found in tomography models [*Thorne et al.*, 2004], our inferred  $\delta V_S$  displays complexity and a transition from relatively high to low velocities over a much smaller lateral scale than the tomography models. This observed lateral shear velocity gradient is best matched by TXBW, which depicts a velocity transition occurring over the shortest lateral scale length (approximately 600–1200 km).

[14] Since  $\delta V_S$  values were derived from averaging  $\delta T_{S-SKS}$  along whole D'' ray paths and plotted at path midpoints, we will underestimate and mislocate  $\delta V_S$  heterogeneity in the likely case that velocity structure along the ray path has shorter-wavelength variations than the D'' path length. It is also important to point out the uncertainty relating to ray path dependence on the vertical D'' velocity gradient [*Ritsema et al.*, 1997]. To further explore the spatial velocity trends, we calculate a moving cap average of  $\delta V_S$  throughout the study area as in study by *Wyession* [1996]. The cap-averaged results accentuate a velocity increase from northwest to southeast, but serve to mute the complexity in the center of the study area (see auxiliary material). Cap-averaging the velocity heterogeneity agrees best with model TXBW. North-south cross sections offer a more detailed, though heavily model-dependent, inspection of  $\delta V_S$  in D'' (Figure 6). The transitional region from velocities greater than PREM in the southeast to depressed velocities in the northwest is readily apparent, and occurs over a fairly small-scale lateral (north-south) dimension of approximately 250–500 km. The travel time data alone are not able to constrain whether this transition is discontinuous (as reported by *Ni et al.* [2005]). The cross sections help to decipher the apparent overlapping of high and low velocities when viewing the

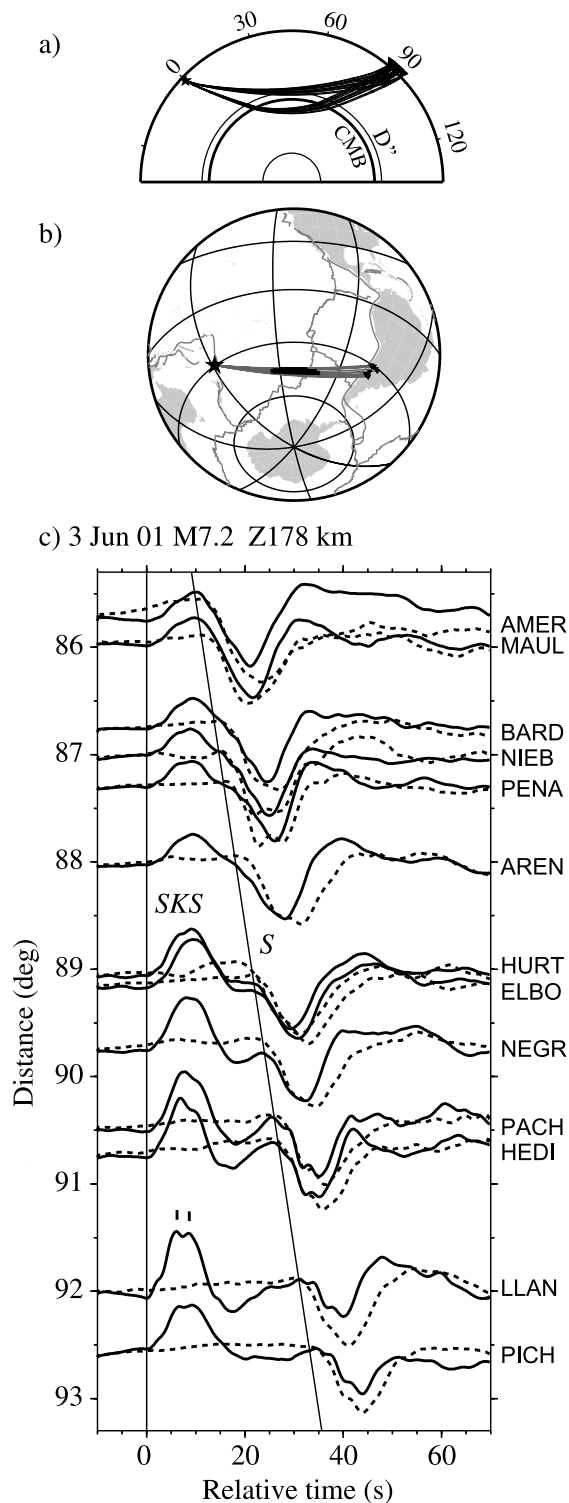


**Figure 2.** The 3 June 2001 event recorded by stations of the CHARGE experiment [*Beck et al.*, 2001]. (a) PREM-calculated *S* and *SKS* ray paths in a cross section along the great circle path from the event to CHARGE stations. (b) Same symbols as Figure 1b with event and CHARGE station geometry. (c) Distance profile of *SV* (solid lines) and *SH* (dashed lines) component waveforms from CHARGE stations. Traces are normalized in time to the *SKS* arrival and scaled to the maximum amplitude of each trace. The *S* arrival time calculated with PREM is shown relative to the *SKS* arrival time (solid lines). A source effect is highlighted on the *SKS* signal recorded at 92° by station LLAN (Punta de Los Llanos, Argentina).

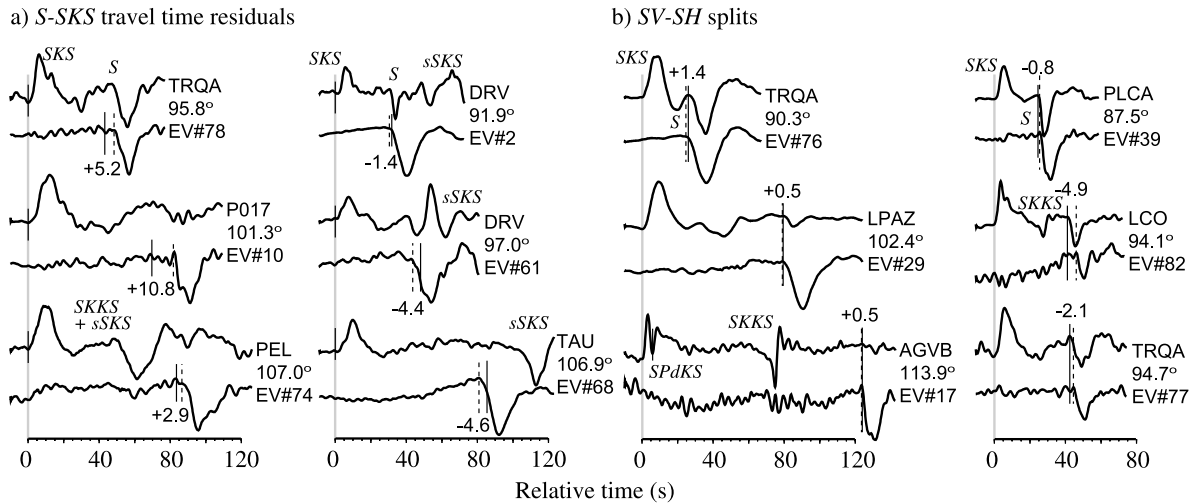


**Figure 3.** (a) Examples of waveforms used in the  $S$ - $SKS$  differential travel time residual ( $\delta T_{S-SKS}$ ) analysis. The dashed lines show hand-picked  $S_{SH}$  arrivals, and the solid lines are the PREM-predicted  $S$  arrival time relative to the handpicked  $SKS$  arrival (light grey line). Values of  $\delta T_{S-SKS}$  are below  $S$  arrivals. Top trace of each pair is the  $SV$  component, bottom trace is  $SH$ . Station, distance, and event number corresponding to Table 1 are listed to the right of each pair of traces. (b) Examples of waveforms used in the shear wave splitting ( $T_{SV-SH}$ ) analysis. The dashed lines show  $S_{SH}$  arrivals, and solid lines mark  $S_{SV}$  onsets. Splitting times are above  $S$  arrivals. Traces are normalized in time to the  $SKS$  arrival and scaled to the maximum amplitude of each trace.

residuals in map view (Figure 5), through the suggestion that deeper low velocities are overlain with high velocities (e.g., the A–A' cross section in Figure 6). However, as mentioned above, this is not well-constrained due to the fact that our  $\delta V_S$  estimates are based on a  $D''$  path-averaging approach.

[15] Trends in  $\delta T_{SKKS-SKS}$  were investigated to explore possible heterogeneity patterns away from the center of our  $S$  ray paths, and more toward locations where  $SKS$  traverses  $D''$ . As noted earlier, significant  $\delta T_{SKKS-SKS}$  remain even after correction for heterogeneity predicted by tomography throughout the mantle (Figure 4b). The geographic distribution of  $\delta T_{SKKS-SKS}$  at CMB entry and exit points agrees with the trend in the tomography model SAW24B16, though the amplitude of the anomaly is not well matched (see auxiliary material). Most of the westerly  $D''$  paths center in a low-velocity region, while the eastern deep mantle paths traverse average to higher-than-average velocity structure. A majority of the  $SKKS$ - $SKS$  residuals are positive, implying (in a relative sense) either an early  $SKS$  or delayed  $SKKS$ . While positive  $\delta T_{SKKS-SKS}$  can arise by a 1-D reduction in shear velocity,  $SKKS$  delays relative to  $SKS$  are most effectively induced by lateral heterogeneity or strong lateral gradients between the  $SKKS$  and  $SKS$  at  $D''$  sampling locations. Therefore the large observations of  $\delta T_{SKKS-SKS}$  are best matched when there is anomalous velocity structures in the region between  $SKS$  and  $SKKS$  sampling locations, at the eastern and western borders of our sample region. In fact, Tanaka [2002] reports a 5–7% low-velocity region in this same area (Figure 1a, region 2). It is also possible that the low-velocity region in our study area extends farther east than predicted by tomography, such that  $SKKS$  samples this structure, but  $SKS$  does not. This would explain the fairly constant high amplitudes of  $\delta T_{SKKS-SKS}$  at all distances and latitudes north of approximately 48°S and require a

large decrease in velocity over the small lateral distance between  $SKS$  and  $SKKS$  sample locations in the eastern part of the southern Pacific region.

## 4. Shear Wave Velocity Anisotropy

### 4.1. Shear Wave Splitting Times

[16] Our entire data set was inspected for the differential travel time between  $S_{SV}$  and  $S_{SH}$  arrivals ( $T_{SV-SH}$ ). This differential travel time is also referred to as the shear wave splitting time (or shear wave splits). We used data that had both radial and transverse energy, a good signal-to-noise ratio, impulsive sources, and the absence of surface reflected  $SKS$  or  $SKKS$  energy. This selection criteria resulted in 170 splitting measurements. Cross correlation of the phases was not used to measure  $T_{SV-SH}$  due to the amplitude difference and waveform variability of the  $SV$  and  $SH$  components of diffracted  $S$  [Teng and Richards, 1968]. Also, as anisotropy has been shown to exist in the outer few hundred km of the Earth (e.g., see reviews by Savage [1999] and Silver [1996]), data used to study deep mantle anisotropy must first be corrected for these effects. To correct for possible receiver-side anisotropy, we use previously calculated upper mantle anisotropy parameters for stations in this study (referenced in Table 2). The traces are rotated to the reported station fast polarization direction, time shifted by the reported splitting time, then rotated back to the great circle path coordinate system. The arrival times of  $S_{SV}$  and  $S_{SH}$  were measured by hand-picking the phase onset. We assign our maximum measurement error to be  $\pm 1$  s (the highest-quality data are more likely within  $\pm 0.5$  s), though we acknowledge that assessment of travel time picking error is somewhat subjective. The shear wave splits are summarized in Figure 4c and range from  $-6$  s (early  $S_{SV}$  relative to  $S_{SH}$ ) to 5 s (delayed  $S_{SV}$  relative to

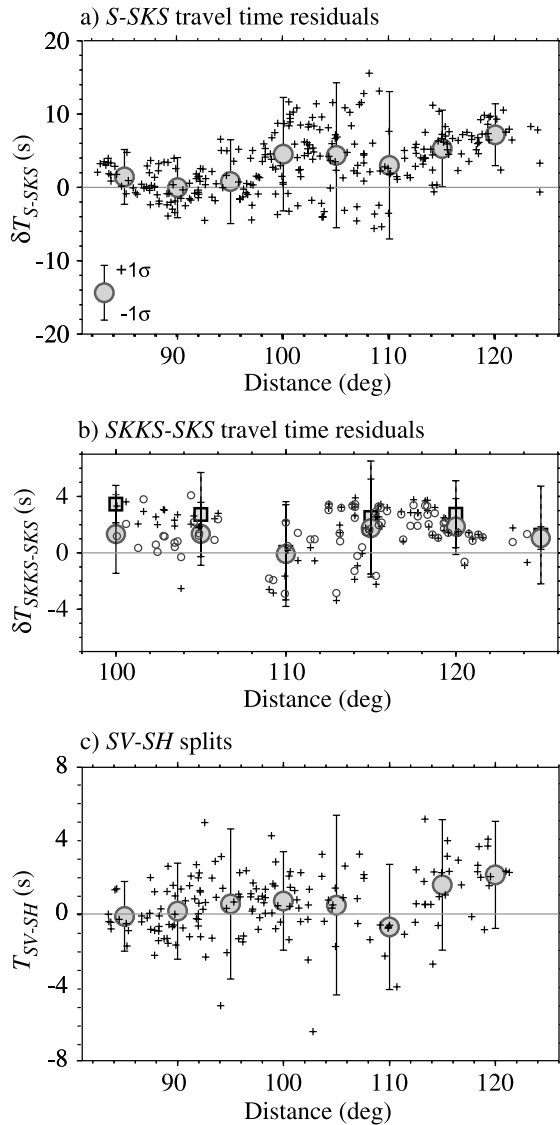


**Figure 4.** (a) The  $\delta T_{S-SKS}$  (observed  $S$ - $SKS$  differential travel time minus PREM-predicted  $S$ - $SKS$  differential travel time) versus distance (crosses) and  $5^\circ$  distance bin averages (larger circles). Error bars represent  $\pm 1$  standard deviation in each distance bin. (b) The  $\delta T_{SKKS-SKS}$  (observed  $SKKS$ - $SKS$  differential travel time minus PREM-predicted  $SKKS$ - $SKS$  differential travel time) versus distance. Residuals before (crosses) and after (circles) correction for 3-D mantle heterogeneity by the model, SAW24B16 [Mégnin and Romanowicz, 2000] are shown. The averages of  $5^\circ$  distance bins (large squares and circles for uncorrected and corrected residuals, respectively) are also shown, along with  $\pm 1$  standard deviation error bars. (c)  $T_{SV-SH}$  (shear wave splits) versus distance (crosses) and  $5^\circ$  distance bin averages (circles). Error bars as in Figure 4a.

$S_{SH}$ ). These times have a mild suggestion of increasing splitting time with distance, which is expected for increasing path lengths in an anisotropic  $D''$  layer [e.g., Fouch et al., 2001; Moore et al., 2004]. However, there is significant scatter, which is consistent with strong variability in the properties of  $D''$  anisotropy.

## 4.2. Inferred $D''$ Anisotropy

[17] We infer  $D''$  anisotropy by assuming the observed splitting time was uniformly accrued along the PREM-predicted ray path in a 300 km thick  $D''$  layer. We define percent anisotropy  $k_S$  as

$$k_S = 100 \frac{V_{SH} - V_{SV}}{V_{SH}}, \quad (1)$$

where  $V_{SH}$  and  $V_{SV}$  are the velocities of  $S_{SH}$  and  $S_{SV}$ , respectively. Our  $k_S$  estimates range from  $-1.0$  to  $+0.9\%$ . Analysis of the geographic distribution of  $T_{SV-SH}$  at ray path midpoints shows a slight trend of positive splitting times ( $S_{SV}$  arrives after  $S_{SH}$ ) in the east and negative splitting times ( $S_{SV}$  arrives before  $S_{SH}$ ) in the west, with some considerable overlap and complexity in the center of the study region (Figure 5e). We compare our  $k_S$  estimates with the anisotropy tomography model, SAW24AN16 (Panning and Romanowicz, submitted manuscript, 2005), the only global  $D''$  anisotropy study to date (Figure 5f). SAW24AN16 shows positive  $k_S$  in the north and east of the study region and weak anisotropy in the center, where the midpoints of our ray paths cluster and display highly variable  $k_S$ . SAW24AN16 and our study appear to produce contrasting results, though we note that this model used much longer period data, and hence emphasizes much larger-scale perturbations.

[18] The majority of past regional studies of  $D''$  anisotropy document the predominance of positive  $T_{SV-SH}$  (thus positive  $k_S$ ) [e.g., Garnero and Lay, 1997, 2003; Kendall and Silver, 1996b; Ritsema, 2000; Ritsema et al., 1998; Thomas and Kendall, 2002; Usui et al., 2005]. The most common interpretation of this behavior is that it is caused by vertical transverse isotropy (VTI, i.e., transverse isotropy with a vertical axis of symmetry) [see Moore et al., 2004]. Regions of relatively weak or no deep mantle shear wave splitting have also been reported [Garnero et al., 2004; Kendall and Silver, 1996a]. These regions may only be weakly strained, without overlying subduction or plume upwelling. Kendall and Silver [1996a] report one such region of weak anisotropy in an east-west corridor across the center of our study area (Figure 1a, region 1). This is compatible with some of our observations which have small splitting times. However, we see evidence for significant shear wave splitting in many of our data; thus  $D''$  anisotropy is present through most of this region.

[19] The range and magnitude of the positive  $T_{SV-SH}$  values presented here are similar to those reported elsewhere; however, our large negative  $T_{SV-SH}$  splitting times are unusual. Some studies have noted geographically isolated zones where  $S_{SV}$  arrives before  $S_{SH}$  (i.e., negative  $T_{SV-SH}$  and  $k_S$ ) [Pulliam and Sen, 1998; Russell et al., 1999], but  $T_{SV-SH}$  is only between  $-2$  and  $-1.5$  s. Such a range of observations requires a change in the symmetry of the anisotropy. Two likely candidates are transverse isotropy with a horizontal axis of symmetry, or azimuthal anisotropy, though the former is essentially a form of the latter. Unfortunately, due to the station and event locations, our data sample  $D''$  at restricted azimuths, thus we are unable to assess any dependency of  $k_S$  on ray path direction and constrain possible mechanisms of azimuthal anisotropy.

[20] Relatively little has been established regarding possible contribution of source-side upper mantle anisotropy

to lower mantle splitting measurements, but some recent work has found evidence for anisotropy in the upper mantle below the southwest Pacific [Wookey and Kendall, 2004]. Source-side anisotropy may indeed contribute to some of the scatter observed in  $k_S$ . However, inspecting dependency of  $T_{SV-SH}$  times on earthquake source depth reveals little systematic bias or trend. We thus infer that upper mantle anisotropy is not dominating our deep mantle anisotropy signal.

## 5. Discussion

### 5.1. Correlation of Velocity and Anisotropy Heterogeneity

[21] Previous studies have noted a weak positive correlation between anisotropy and velocity [Garnero and Lay, 2003; Rokesky et al., 2004]. However, the majority of observations in these studies inferred positive  $\delta V_S$  and  $k_S$ . As previously stated, our southern Pacific region extends over a large area, and has both positive and negative velocity perturbations and variable inferred anisotropy strength. We compared data where both  $\delta T_{S-SKS}$  and  $T_{SV-SH}$  are measured and found no clear correlation between estimates of heterogeneity and anisotropy. We also compared  $\delta V_S$  and  $k_S$  for every  $4^\circ$  of our cap-averaged results and again, found no clear positive correlation (see auxiliary material). Thermochemically heterogeneous material in the presence of variable strain could produce the low correlation observed here and will be discussed later in a geodynamical context. An important assumption in studies utilizing  $S_{SH}$ - $S_{KS}$  differential travel times is that results interpret isotropic  $V_{SH}$  structure, or the faster shear wave velocity in a VTI system. However, in the presence of both anisotropy and velocity heterogeneity this assumption can lead to error in the interpreted velocity structure, since variable anisotropic velocity will likely contribute to the  $S_{SH}$ - $S_{KS}$  differential travel time because the phases are measured on different components of motion. Nonetheless, mapping the lateral variations in the differential travel times remains important, as it relates to scales of heterogeneity and dynamical processes.

### 5.2. Lateral Velocity Gradient Analysis

[22] We examined the variable  $\delta V_S$  near the center of our study region in greater detail and found that  $\delta T_{S-SKS}$  versus ray path midpoint latitude reveals a south-to-north trend, where residuals appear to rapidly increase near  $50^\circ\text{S}$  (see auxiliary material). This is also apparent in the path length normalized  $\delta V_S$ , plotted against ray path midpoint latitude,

where a change of almost 1.5%  $\delta V_S$  occurs over a fairly short lateral scale length less than approximately 600 km along the CMB. This strong shear velocity lateral gradient is greater than in any of the tomographic models compared here. A strong transition into reduced shear velocities has been modeled as vertical boundaries at the base of the mantle beneath southern Africa [Ni et al., 2005, 2002], which is the other degree-two low-velocity deep mantle region.

[23] Our  $\delta V_S$  analysis relies heavily on 1-D approximations of ray paths and travel time predictions from the PREM model. Others have noted that sharp boundaries create two-dimensional (2-D) [Wen, 2002] and 3-D [Ni et al., 2005] effects, such as phase multiples and multipathing. Thus, to more definitively assess the presence of sharp transitional velocities, we examine the waveforms for evidence of these effects. In order to directly compare waveforms produced by different events, 62 traces with the simplest and most impulsive  $S_{KS}$  phases were selected (22% of the data set). The  $S_{SH}$  waveform of those traces was then inspected at its relative peak time versus ray path midpoint latitude (Figure 7a). Several traces exhibit complex waveform behavior, such as shoulders in  $S$  due to multipathing (open inverted triangle in Figure 7a) and possible phase triplications (solid inverted triangle in Figure 7a). To clear up the analysis and accentuate small, robust effects, we stack the waveforms by summing the normalized traces in  $2^\circ$  latitude bins (Figure 7b). The shoulders and possible multiples are evident, but there is no latitudinal trend to the waveform behavior. There is, however, a trend in phase arrival time and waveform character versus ray path midpoint latitude when the traces are plotted relative to the  $S$  arrival time predicted by PREM and corrected with the travel time perturbations predicted by SAW24B16 to a depth of 2591 km (Figure 7c). This trend is even more evident when the traces are stacked in  $2^\circ$  latitude bins (Figure 7d). The phase arrival time (relative to SAW24B16 corrected PREM) and waveform shape is fairly consistent up to a latitude of approximately  $53^\circ\text{S}$ , but near  $51^\circ\text{S}$  the relative arrival time shifts slightly and begins to increase linearly. The waveform also gains complexity. This region of transitional waveform behavior occurs over a few degrees in latitude with a scale length less than 300 km at the CMB. North of this latitude the phases continue the linear trend in arrival time delay and waveforms display intermittent complexity with latitude. We examined traces with complex waveform behavior in distance and azimuth profiles by event. Unfortunately, events that produced the most characteristic edge effects in the waveforms were only

**Figure 5.** (a) The  $\delta T_{S-SKS}$  plotted at ray path midpoints for the region outlined in the inset globe. (b–d) The  $\delta V_S$  heterogeneity inferred from corrected  $\delta T_{S-SKS}$ . The  $\delta V_S$  is plotted on, and corrected by, the D'' velocity models: TXBW [Grand, 2002] (Figure 5b); S20RTS [Ritsema and van Heijst, 2000] (Figure 5c); and SAW24B16 [Mégnin and Romanowicz, 2000] (Figure 5d). Contour lines are plotted in 0.4% (dashed lines) and 0.8% (solid lines) intervals, with red and blue corresponding to low and high velocities, respectively, and black indicating no velocity perturbation. The amplitudes of  $\delta V_S$  from tomography and travel time observations are similar, but the lateral velocity gradient from fast (or average) velocity to relatively slow is much greater in the observations than in the tomography. (e)  $T_{SV-SH}$  (splitting times) plotted as in Figure 5a. (f) D'' anisotropy,  $k_S$ , inferred from  $T_{SV-SH}$ , plotted on the global D'' anisotropy model, SAW24AN16 (Panning and Romanowicz, submitted manuscript, 2005). Contour lines are plotted in 0.25% (dashed lines) and 0.5% (solid lines) intervals, with red and blue corresponding to  $V_{SV} > V_{SH}$  and  $V_{SV} < V_{SH}$ , respectively, and black indicating isotropy. Anisotropy is highly variable along the center of the region.

recorded with high quality by a small number of stations (Table 1). When high-quality data are available for an event recorded at multiple stations, we often observe anomalous *SKS* shape at distances where *SKS* is predicted to be free from interfering phases (Figure 2c). At these distances *SKS* can detect anomalous source or receiver effects, and care

must be used to interpret anomalous *S* waveforms when *SKS* is also anomalous, since the effects may be unrelated to lower mantle structure. So, although there is waveform evidence for sharp boundary-like structure in the lower mantle of our study region, we are unable to fully constrain the location and shape of it. However, the anomalous

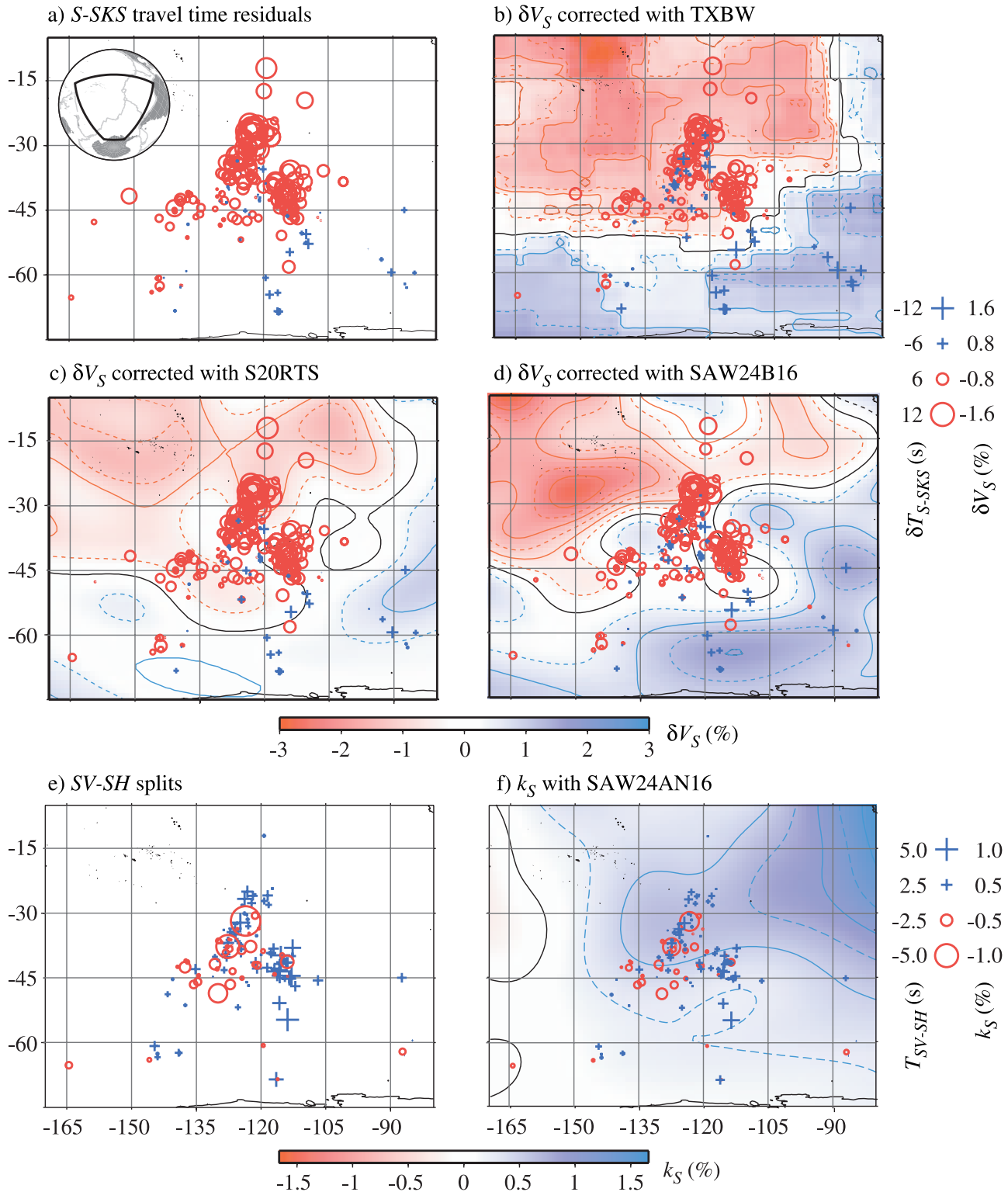
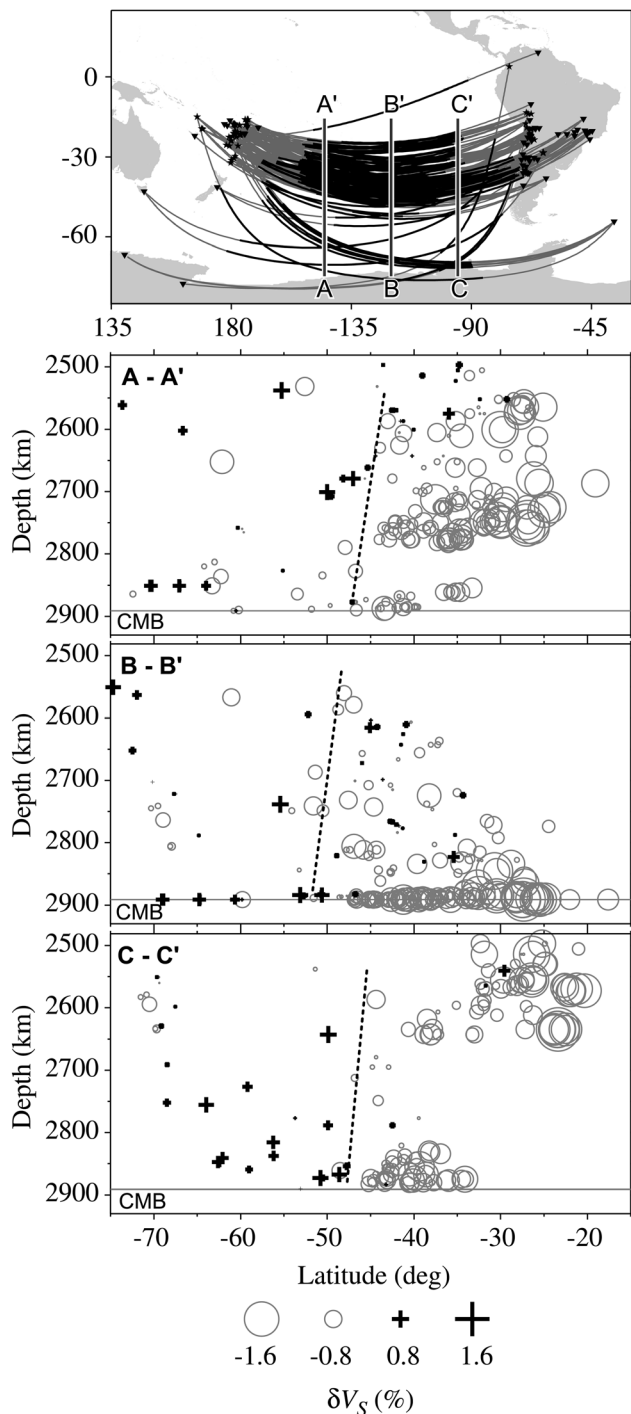


Figure 5



**Figure 6.** (top) Map displaying event (star)-receiver (inverted triangle) geometry, along with great circle ray paths, where D'' portions of paths are thicker. Also shown are three north-south cross sections, which correspond to depth cross sections displayed in the bottom three panels. Heterogeneity estimates ( $\delta V_S$ ) are plotted at PREM-predicted locations where ray paths penetrate each cross section. Thin nearly vertical dashed lines in the cross sections denote interpretation of approximate location of abrupt transition from low-to-high shear wave speeds.

structure is most probably near 52°S beneath the southern Pacific.

### 5.3. Geodynamic Implications

[24] There is growing evidence that the large low-velocity seismic anomaly beneath Africa may be due to lower mantle chemical heterogeneity [e.g., *Ni and Helmberger*, 2003a, 2003b; *Ritsema*, 2000; *Wang and Wen*, 2004; *Wen*, 2001]. A chemical origin for the Pacific anomaly has also been inferred [e.g., *Ishii and Tromp*, 1999, 2004; *Trampert et al.*, 2004]. *McNamara and Zhong* [2005] recently performed a thermochemical convection study to investigate the predicted geometry of a dense mantle component at the base of the mantle as influenced by Earth's plate tectonic history from the Cretaceous to the present-day. Several calculations were performed for different initial volumes of a dense mantle component with a density 2–5% higher than the less dense mantle material. The dense component was allowed to deform in the flow field generated by 11 stages of inferred plate history for the past 119 Myr [*Lithgow-Bertelloni and Richards*, 1998]. It was found that the dense material typically forms two large anomalous features: a ridge-like northwest-southeast trending structure beneath Africa and a more rounded anomaly beneath the Pacific. Both features geometrically resemble to first-order the large low-velocity anomalies in the lower mantle. In addition, these predicted anomalies have distinct edges and are substantially hotter than the surrounding material, providing sharp contrasts in both temperature and composition along their boundaries. A more subtle point is that if the African anomaly is compositional in nature and has sharp contacts, then geodynamical modeling predicts that a Pacific compositional anomaly with well-defined edges should also exist.

[25] Figure 8 shows the predicted present-day geometry of an initially 255 km thick dense layer after 119 Myr of plate motion history. Circum-Pacific subduction has swept dense material into a series of overlapping ridges, forming a large, hot compositional anomaly beneath the Pacific. A limb of the predicted compositional anomaly extends into the study region. It is expected that shear waves entering this limb would encounter sharp transitions in both temperature and composition. Note that a possible more dense component within the Earth's lower mantle may not have the same volume as that shown in Figure 8; however, geodynamical calculations starting with different initial volumes of more dense material all predict the presence of a southeast limb extending into the study region. This is one possible origin to the sharp shear velocity transition discussed here.

[26] Seismic anisotropy is typically attributed to either lattice-preferred orientation (LPO) or shape-preferred orientation (SPO) [*Karato*, 1998a, 1998b]. Both mechanisms may be present in this study region due to its location, which is in an intermediate tectonic regime, away from subduction and large-scale regional upwelling, and possibly encompassing the boundary of a large Pacific chemical anomaly. The development of LPO is dependent upon the strain that material undergoes when it is deforming by dislocation creep, and geodynamical predictions indicate that strain patterns may become quite complicated away from subducting slabs [*McNamara et al.*, 2003], especially

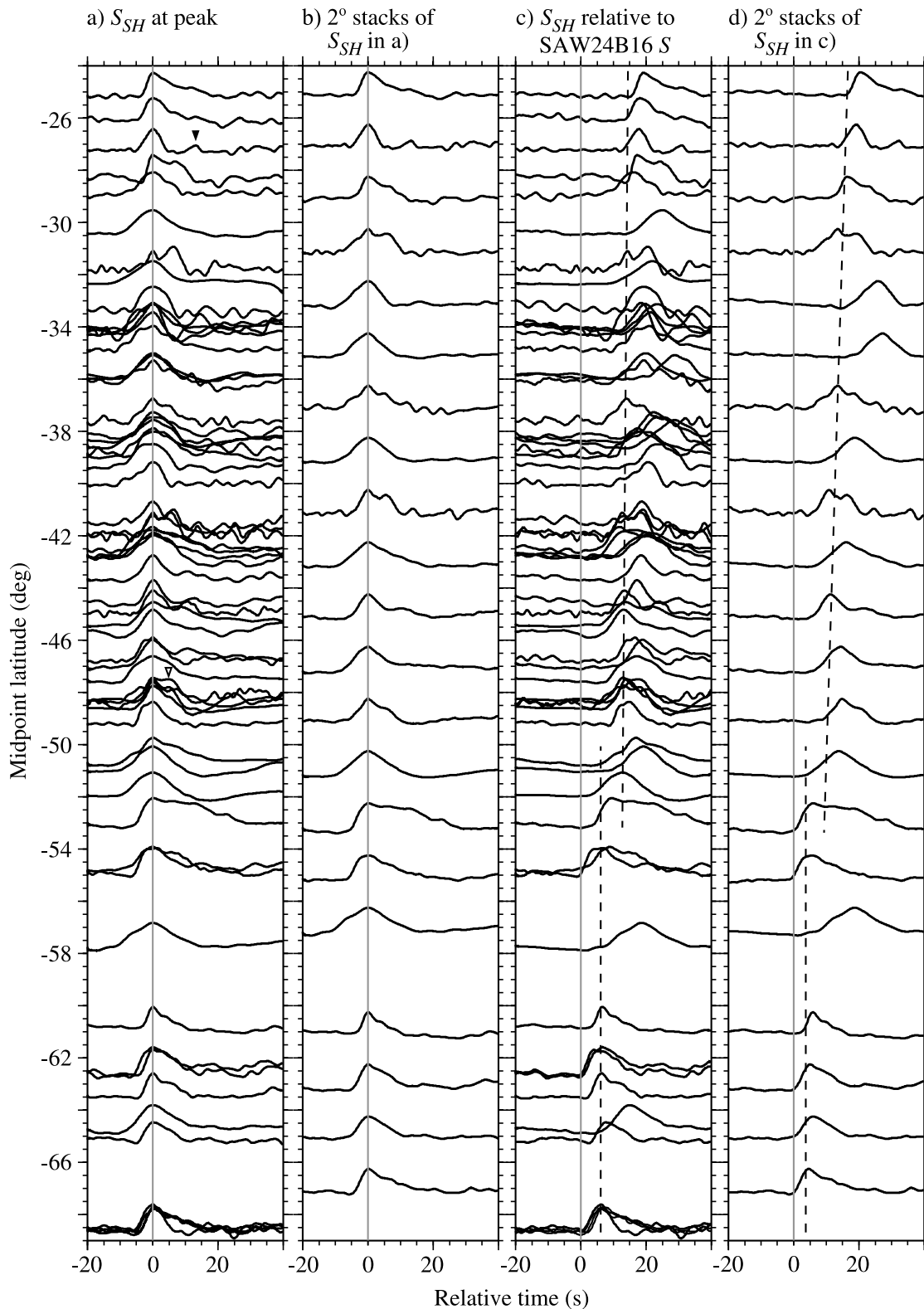


**Figure 7.** Ray path midpoint latitude profiles, where only waveforms (scaled to the maximum amplitude in each trace) with very simple, impulsive  $SKS$  are plotted. (a)  $SH$  component waveforms plotted relative to the peak of  $S$ . Possible phase multipathing (open inverted triangle) and multiples (solid inverted triangle) are present. (b) Traces in Figure 7a stacked for every  $2^\circ$  of latitude by summing each of the scaled traces and dividing by the total number of traces. (c) Traces in Figure 7a plotted relative to the PREM-predicted and SAW24B16-corrected  $S$  arrival time. Dashed lines mark linear trend in  $S$  arrival times. Note the change in slope and waveform character between  $53^\circ S$  and  $51^\circ S$ . (d) The same traces as in Figure 7c stacked as in Figure 7b.

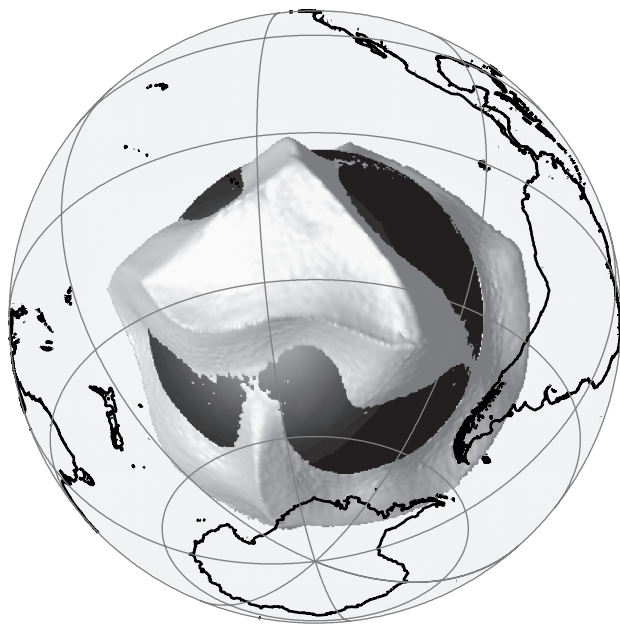


**Figure 8.** Geodynamical snapshot of the compositional field resulting from 119 Myr of Earth's plate history imposed upon an initially 255 km thick more dense layer [McNamara and Zhong, 2005]. The projection is centered on the same region as Figure 1. The core is black. Shown in light gray is the compositional isosurface marking the sharp, density interface. A southeast limb of the more dense material projects into the study area. Present-day coastlines are shown at the surface.

if  $D''$  is characterized by small-scale convection [Solomatov and Moresi, 2002]. There is a lack of geodynamical investigation on the development of SPO anisotropy, however, and if the study region includes the edge of a hot, compositional anomaly, then SPO arising from partial melting and/or chemical heterogeneity should not be ruled out. It is not unexpected that both possible mechanisms would generate complicated seismic anisotropy patterns in this region. These patterns would not provide easily interpretable constraints upon mantle dynamics and could explain the variations in seismic anisotropy observed in this study.

## 6. Conclusions

[27] High quality broadband records of 60 southwest Pacific and 23 South American earthquakes from 87 temporary and permanent seismic stations allow a regional investigation of  $D''$  velocity and anisotropy heterogeneity beneath a large portion of the southern Pacific for the first time. The analysis of 276  $S$ -SKS differential travel time residuals, ranging from  $-6$  to  $15.5$  s, reveals a large south-to-north lateral velocity gradient beginning at approximately  $53^\circ\text{S}$ , where inferred velocity perturbations decrease from approximately  $0.5\%$  to  $-1.0\%$  over less than  $600$  km along the CMB. The addition of 73 SKKS-SKS differential travel time residuals helps to constrain the possible location of this transitional region. Current long-wavelength tomography models do not render such a strong lateral transition in

velocities. There is evidence in the waveforms for an even smaller lateral transition region that is less than  $300$  km along the CMB. Some waveforms display effects of steeply dipping boundaries at the initiation of this lateral gradient; however, the results are not conclusive. A new geodynamical model of density anomalies at the base of the mantle predicts the presence of a compositionally distinct region with well-defined edges in the study area. The mostly east-to-west ray paths of the data preclude further constraints on the geometry of the lateral velocity gradient or the location of the possible sharp boundaries. The shear wave splitting time between  $S_{SH}$  and  $S_{SV}$  was measured on 170 traces. The majority of the splitting times were between  $-3$  and  $5.2$  s.  $D''$  shear wave splitting behavior is highly variable, though there is a slight spatial trend where the  $S_{SH}$  arrives earlier than  $S_{SV}$  in the north and east part of the study area, and later than  $S_{SV}$  in the center and southwest of it. This is the first observation of a complex pattern of positive and negative splitting times over such short scales. The observations of anisotropy and velocity heterogeneity in  $D''$  beneath the southern Pacific could be explained by thermochemical heterogeneity at the boundary of the Pacific Superswell, as well as small-scale convection in the deep mantle.

[28] **Acknowledgments.** The IRIS Data Management Center provided the majority of the waveforms used in this study. Susan Beck and Doug Wiens allowed us early access to the CHARGE and TAMSeis data sets, respectively. Peter Burkett provided the CIW data sets from the BLSP and PISCO experiments with the assistance of Matt Fouch. The International Seismic Network of NIED gave access to SPANET data. Charles Mégnin, Steve Grand, Jeroen Ritsema, and Mark Panning provided the inversion coefficients for their respective tomographic models. Most signal analysis was done with SAC [Goldstein *et al.*, 1999], travel time analysis was aided by the TauP Toolkit [Crotwell *et al.*, 1999], and figures were made using GMT [Wessel and Smith, 1998]. This research was supported by NSF grant EAR-0135119.

## References

- Anderson, M. L., G. Zandt, E. Triep, M. Fouch, and S. Beck (2004), Anisotropy and mantle flow in the Chile-Argentina subduction zone from shear wave splitting analysis, *Geophys. Res. Lett.*, *31*(23), L23608, doi:10.1029/2004GL020906.
- Antolik, M., Y. J. Gu, G. Ekstrom, and A. M. Dziewonski (2003), J362D28: A new joint model of compressional and shear velocity in the Earth's mantle, *Geophys. J. Int.*, *153*, 443–466.
- Audoine, E., M. K. Savage, and K. Gledhill (2000), Seismic anisotropy from local earthquakes in the transition region from a subduction to a strike-slip plate boundary, New Zealand, *J. Geophys. Res.*, *105*(B4), 8013–8034.
- Barruol, G., and R. Hoffmann (1999), Upper mantle anisotropy beneath the Geoscope stations, *J. Geophys. Res.*, *104*(B5), 10,757–10,774.
- Beck, S., *et al.* (2001), CHARGE, the Chile Argentina Geophysical Experiment, Imaging the south central Andean lithosphere using passive broadband seismology, *Eos Trans. AGU*, *82*(47), Fall Meet. Suppl., Abstract T31A-0828.
- Bock, G., R. Kind, A. Rudloff, and G. Asch (1998), Shear wave anisotropy in the upper mantle beneath the Nazca plate in northern Chile, *J. Geophys. Res.*, *103*(B10), 24,333–24,346.
- Bullen, K. E. (1949), Compressibility-pressure hypothesis and the Earth's interior, *Mon. Not. R. Astron. Soc., Geophys. Suppl.*, *5*, 355–368.
- Choy, G. L., and P. G. Richards (1975), Pulse distortion and Hilbert transformation in multiply reflected and refracted body waves, *Bull. Seismol. Soc. Am.*, *65*, 55–70.
- Christensen, U. R., and P. Olson (2003), Secular variation in numerical geodynamo models with lateral variations of boundary heat flow, *Phys. Earth Planet. Inter.*, *138*, 39–54.
- Crotwell, H. P., T. J. Owens, and J. Ritsema (1999), The TauP Toolkit: Flexible seismic travel-time and ray-path utilities, *Seismol. Res. Lett.*, *70*, 154–160.
- Dziewonski, A. M., and D. L. Anderson (1981), Preliminary reference Earth model, *Phys. Earth Planet. Inter.*, *25*, 297–356.

- Fischer, K. M., and D. A. Wiens (1996), The depth distribution of mantle anisotropy beneath the Tonga subduction zone, *Earth Planet. Sci. Lett.*, *142*, 253–260.
- Fisher, J. L., M. E. Wysession, and K. M. Fischer (2003), Small-scale lateral variations in D'' attenuation and velocity structure, *Geophys. Res. Lett.*, *30*(8), 1435, doi:10.1029/2002GL016179.
- Fouch, M. J., K. M. Fischer, and M. E. Wysession (2001), Lowermost mantle anisotropy beneath the Pacific: Imaging the source of the Hawaiian plume, *Earth Planet. Sci. Lett.*, *190*, 167–180.
- Garnero, E. J. (2000), Heterogeneity of the lowermost mantle, *Annu. Rev. Earth Planet. Sci.*, *28*, 509–537.
- Garnero, E. J., and D. V. Helmberger (1995), A very slow basal layer underlying large-scale low-velocity anomalies in the lower mantle beneath the Pacific: Evidence from core phases, *Phys. Earth Planet. Inter.*, *91*, 161–176.
- Garnero, E. J., and T. Lay (1997), Lateral variations in lowermost mantle shear wave anisotropy beneath the north Pacific and Alaska, *J. Geophys. Res.*, *102*(B4), 8121–8136.
- Garnero, E. J., and T. Lay (2003), D'' shear velocity heterogeneity, anisotropy and discontinuity structure beneath the Caribbean and Central America, *Phys. Earth Planet. Inter.*, *140*, 219–242.
- Garnero, E. J., S. P. Grand, and D. V. Helmberger (1993), Low P-wave velocity at the base of the mantle, *Geophys. Res. Lett.*, *20*, 1843–1846.
- Garnero, E. J., M. M. Moore, T. Lay, and M. J. Fouch (2004), Isotropy or weak vertical transverse isotropy in D'' beneath the Atlantic Ocean, *J. Geophys. Res.*, *109*, B08308, doi:10.1029/2004JB003004.
- Glatzmaier, G. A. (2002), Geodynamo simulations: How realistic are they?, *Annu. Rev. Earth Planet. Sci.*, *30*, 237–257.
- Goldstein, P., D. Dodge, and M. Firpo (1999), SAC2000: Signal processing and analysis tools for seismologists and engineers, in *International Handbook of Earthquake and Engineering Seismology, Part B, Int. Geophys.*, vol. 81B, edited by W. Lee et al., pp. 1613–1614, Elsevier, New York.
- Grand, S. P. (2002), Mantle shear-wave tomography and the fate of subducted slabs, *Philos. Trans. R. Soc. London, Ser. A*, *360*, 2475–2491.
- Helffrich, G., D. A. Wiens, E. Vera, S. Barrientos, P. Shore, S. Robertson, and R. Adaros (2002), A teleseismic shear-wave splitting study to investigate mantle flow around South America and implications for plate-driving forces, *Geophys. J. Int.*, *149*, F1–F7.
- Ishii, M., and J. Tromp (1999), Normal-mode and free-air gravity constraints on lateral variations in velocity and density of Earth's mantle, *Science*, *285*, 1231–1236.
- Ishii, M., and J. Tromp (2004), Constraining large-scale mantle heterogeneity using mantle and inner-core sensitive normal modes, *Phys. Earth Planet. Inter.*, *146*, 113–124.
- James, D. E., and M. Assumpcao (1996), Tectonic implications of S-wave anisotropy beneath SE Brazil, *Geophys. J. Int.*, *126*, 1–10.
- Karato, S. I. (1998a), Seismic anisotropy in the deep mantle, boundary layers and the geometry of mantle convection, *Pure Appl. Geophys.*, *151*, 565–587.
- Karato, S. I. (1998b), Some remarks on the origin of seismic anisotropy in the D'' layer, *Earth Planets Space*, *50*, 1019–1028.
- Kendall, J.-M. (2000), Seismic anisotropy in the boundary layers of the mantle, in *Earth's Deep Interior: Mineral Physics and Tomography From the Atomic to the Global Scale, Geophys. Monogr. Ser.*, vol. 117, edited by S.-I. Karato et al., pp. 133–159, AGU, Washington, D. C.
- Kendall, J.-M., and P. G. Silver (1996a), Seismic anisotropy in the lower mantle and the fate of subducted slabs, *Eos Trans. AGU*, *77*(46), Fall Meet. Suppl., F708.
- Kendall, J. M., and P. G. Silver (1996b), Constraints from seismic anisotropy on the nature of the lowermost mantle, *Nature*, *381*, 409–412.
- Kuo, B., E. J. Garnero, and T. Lay (2000), Tomographic inversion of S-SKS times for shear velocity heterogeneity in D'': Degree 12 and hybrid models, *J. Geophys. Res.*, *105*(B12), 28,139–28,158.
- Lay, T., Q. Williams, E. Garnero, L. H. Kellogg, and M. E. Wysession (1998a), Seismic wave anisotropy in the D'' region and its implications, in *The Core-Mantle Boundary Region, Geodyn. Ser.*, vol. 28, edited by M. Gurnis et al., pp. 299–318, AGU, Washington, D. C.
- Lay, T., Q. Williams, and E. J. Garnero (1998b), The core-mantle boundary layer and deep Earth dynamics, *Nature*, *392*, 461–468.
- Leidig, M., and G. Zandt (2003), Modeling of highly anisotropic crust and application to the Altiplano-Puna volcanic complex of the central Andes, *J. Geophys. Res.*, *108*(B1), 2014, doi:10.1029/2001JB000649.
- Lithgow-Bertelloni, C., and M. A. Richards (1998), The dynamics of Cenozoic and Mesozoic plate motions, *Rev. Geophys.*, *36*, 27–78.
- Liu, X.-F., and A. M. Dziewonski (1998), Global analysis of shear wave velocity anomalies in the lower-most mantle, in *The Core-Mantle Boundary Region, Geodyn. Ser.*, vol. 28, edited by M. Gurnis et al., pp. 21–36, AGU, Washington, D. C.
- Masters, G., G. Laske, H. Bolton, and A. M. Dziewonski (2000), The relative behavior of shear velocity, bulk sound speed, and compressional velocity in the mantle: Implications for chemical and thermal structure, in *Earth's Deep Interior: Mineral Physics and Tomography From the Atomic to the Global Scale, Geophys. Monogr. Ser.*, vol. 117, edited by S. Karato et al., pp. 63–87, AGU, Washington, D. C.
- McNamara, A. K., and S. Zhong (2005), Thermochemical piles under Africa and the Pacific, *Nature*, *437*, 1136–1139.
- McNamara, A. K., P. E. van Keken, and S. Karato (2003), Development of finite strain in the convecting lower mantle and its implications for seismic anisotropy, *J. Geophys. Res.*, *108*(B5), 2230, doi:10.1029/2002JB001970.
- Mégnin, C., and B. Romanowicz (2000), The three-dimensional shear velocity structure of the mantle from the inversion of body, surface and higher-mode waveforms, *Geophys. J. Int.*, *143*, 709–728.
- Moore, M. M., E. J. Garnero, T. Lay, and Q. Williams (2004), Shear wave splitting and waveform complexity for lowermost mantle structures with low-velocity lamellae and transverse isotropy, *J. Geophys. Res.*, *109*(B2), B02319, doi:10.1029/2003JB002546.
- Ni, S. D., and D. V. Helmberger (2003a), Further constraints on the African superplume structure, *Phys. Earth Planet. Inter.*, *140*, 243–251.
- Ni, S. D., and D. V. Helmberger (2003b), Seismological constraints on the South African superplume; could be the oldest distinct structure on Earth, *Earth Planet. Sci. Lett.*, *206*, 119–131.
- Ni, S. D., E. Tan, M. Gurnis, and D. Helmberger (2002), Sharp sides to the African superplume, *Science*, *296*, 1850–1852.
- Ni, S. D., D. V. Helmberger, and J. Tromp (2005), Three-dimensional structure of the African superplume from waveform modelling, *Geophys. J. Int.*, *161*, 283–294.
- Polet, J., P. G. Silver, S. Beck, T. Wallace, G. Zandt, S. Ruppert, R. Kind, and A. Rudloff (2000), Shear wave anisotropy beneath the Andes from the BANJO, SEDA, and PISCO experiments, *J. Geophys. Res.*, *105*(B3), 6287–6304.
- Pulliam, J., and M. K. Sen (1998), Seismic anisotropy in the core-mantle transition zone, *Geophys. J. Int.*, *135*, 113–128.
- Ritsema, J. (2000), Evidence for shear velocity anisotropy in the lowermost mantle beneath the Indian Ocean, *Geophys. Res. Lett.*, *27*(7), 1041–1043.
- Ritsema, J., and H. J. van Heijst (2000), Seismic imaging of structural heterogeneity in Earth's mantle: Evidence for large-scale mantle flow, *Sci. Progr.*, *83*, 243–259.
- Ritsema, J., E. Garnero, and T. Lay (1997), A strongly negative shear velocity gradient and lateral variability in the lowermost mantle beneath the Pacific, *J. Geophys. Res.*, *102*(B9), 20,395–20,412.
- Ritsema, J., T. Lay, E. J. Garnero, and H. Benz (1998), Seismic anisotropy in the lowermost mantle beneath the Pacific, *Geophys. Res. Lett.*, *25*(8), 1229–1232.
- Rokosky, J. M., T. Lay, E. J. Garnero, and S. A. Russell (2004), High-resolution investigation of shear wave anisotropy in D'' beneath the Cocos Plate, *Geophys. Res. Lett.*, *31*(7), L07605, doi:10.1029/2003GL018902.
- Russell, S. A., T. Lay, and E. J. Garnero (1999), Small-scale lateral shear velocity and anisotropy heterogeneity near the core-mantle boundary beneath the central Pacific imaged using broadband ScS waves, *J. Geophys. Res.*, *104*(B6), 13,183–13,200.
- Russo, R. M., and P. G. Silver (1994), Trench-parallel flow beneath the Nazca plate from seismic anisotropy, *Science*, *263*, 1105–1111.
- Savage, M. K. (1999), Seismic anisotropy and mantle deformation: What have we learned from shear wave splitting?, *Rev. Geophys.*, *37*, 65–106.
- Silver, P. G. (1996), Seismic anisotropy beneath the continents: Probing the depths of geology, *Annu. Rev. Earth Planet. Sci.*, *24*, 385–396.
- Solomatov, V. S., and L.-N. Moresi (2002), Small-scale convection in the D'' layer, *J. Geophys. Res.*, *107*(B1), 2016, doi:10.1029/2000JB000063.
- Sylvander, M., and A. Souriau (1996), Mapping S-velocity heterogeneities in the D'' region, from SmKS differential travel times, *Phys. Earth Planet. Inter.*, *94*, 1–21.
- Tackley, P. J. (2000), Mantle convection and plate tectonics: Toward an integrated physical and chemical theory, *Science*, *288*, 2002–2007.
- Tanaka, S. (2002), Very low shear wave velocity at the base of the mantle under the South Pacific Superswell, *Earth Planet. Sci. Lett.*, *203*, 879–893.
- Teng, T. L., and P. G. Richards (1968), Diffracted SH and SV, *Nature*, *218*, 1154–1162.
- Thomas, C., and J. M. Kendall (2002), The lowermost mantle beneath northern Asia-II. Evidence for lower-mantle anisotropy, *Geophys. J. Int.*, *151*, 296–308.
- Thorne, M. S., and E. J. Garnero (2004), Inferences on ultralow-velocity zone structure from a global analysis of SPdKS waves, *J. Geophys. Res.*, *109*(B8), B08301, doi:10.1029/2004JB003010.
- Thorne, M. S., E. J. Garnero, and S. P. Grand (2004), Geographic correlation between hot spots and deep mantle lateral shear-wave velocity gradients, *Phys. Earth Planet. Inter.*, *146*, 47–63.

- Trampert, J., F. Deschamps, J. Resovsky, and D. Yuen (2004), Probabilistic tomography maps chemical heterogeneities throughout the lower mantle, *Science*, *306*, 853–856.
- Usui, Y., Y. Hiramatsu, M. Furumoto, and M. Kanao (2005), Thick and anisotropic D'' layer beneath Antarctic Ocean, *Geophys. Res. Lett.*, *32*(13), L13311, doi:10.1029/2005GL022622.
- Vasco, D. W., L. R. Johnson, and O. Marques (2003), Resolution, uncertainty, and whole Earth tomography, *J. Geophys. Res.*, *108*(B1), 2022, doi:10.1029/2001JB000412.
- Vidale, J. E., and M. A. H. Hedlin (1998), Evidence for partial melt at the core-mantle boundary north Tonga from the strong scattering of seismic waves, *Nature*, *391*, 682–685.
- Vinnik, L. P., L. I. Makeyeva, A. Milev, and A. Y. Usenko (1992), Global patterns of azimuthal anisotropy and deformations in the continental mantle, *Geophys. J. Int.*, *111*, 433–447.
- Wang, Y., and L. Wen (2004), Mapping the geometry and geographic distribution of a very low velocity province at the base of the Earth's mantle, *J. Geophys. Res.*, *109*(B10), B10305, doi:10.1029/2003JB002674.
- Wen, L. (2002), An SH hybrid method and shear velocity structures in the lowermost mantle beneath the central Pacific and South Atlantic Oceans, *J. Geophys. Res.*, *107*(B3), 2055, doi:10.1029/2001JB000499.
- Wen, L. X. (2001), Seismic evidence for a rapidly varying compositional anomaly at the base of the Earth's mantle beneath the Indian Ocean, *Earth Planet. Sci. Lett.*, *194*, 83–95.
- Wessel, P., and W. H. F. Smith (1998), New, improved version of generic mapping tools released, *Eos Trans. AGU*, *79*(47), 579.
- Wookey, J., and J. M. Kendall (2004), Evidence of midmantle anisotropy from shear wave splitting and the influence of shear-coupled P waves, *J. Geophys. Res.*, *109*, B07309, doi:10.1029/2003JB002871.
- Wysession, M. E. (1996), Large-scale structure at the core-mantle boundary from diffracted waves, *Nature*, *382*, 244–248.
- Wysession, M. E., K. M. Fischer, G. I. Al-eqabi, P. J. Shore, and I. Gurari (2001), Using MOMA broadband array ScS-S data to image smaller-scale structures at the base of the mantle, *Geophys. Res. Lett.*, *28*(5), 867–870.

---

S. R. Ford, Department of Earth and Planetary Science, University of California, Berkeley, 307 McCone Hall 4767, Berkeley, CA 94720-4767, USA. (sean@seismo.berkeley.edu)

E. J. Garnero and A. K. McNamara, Department of Geological Sciences, Arizona State University, Box 871404, Tempe, AZ 85287-1404, USA.